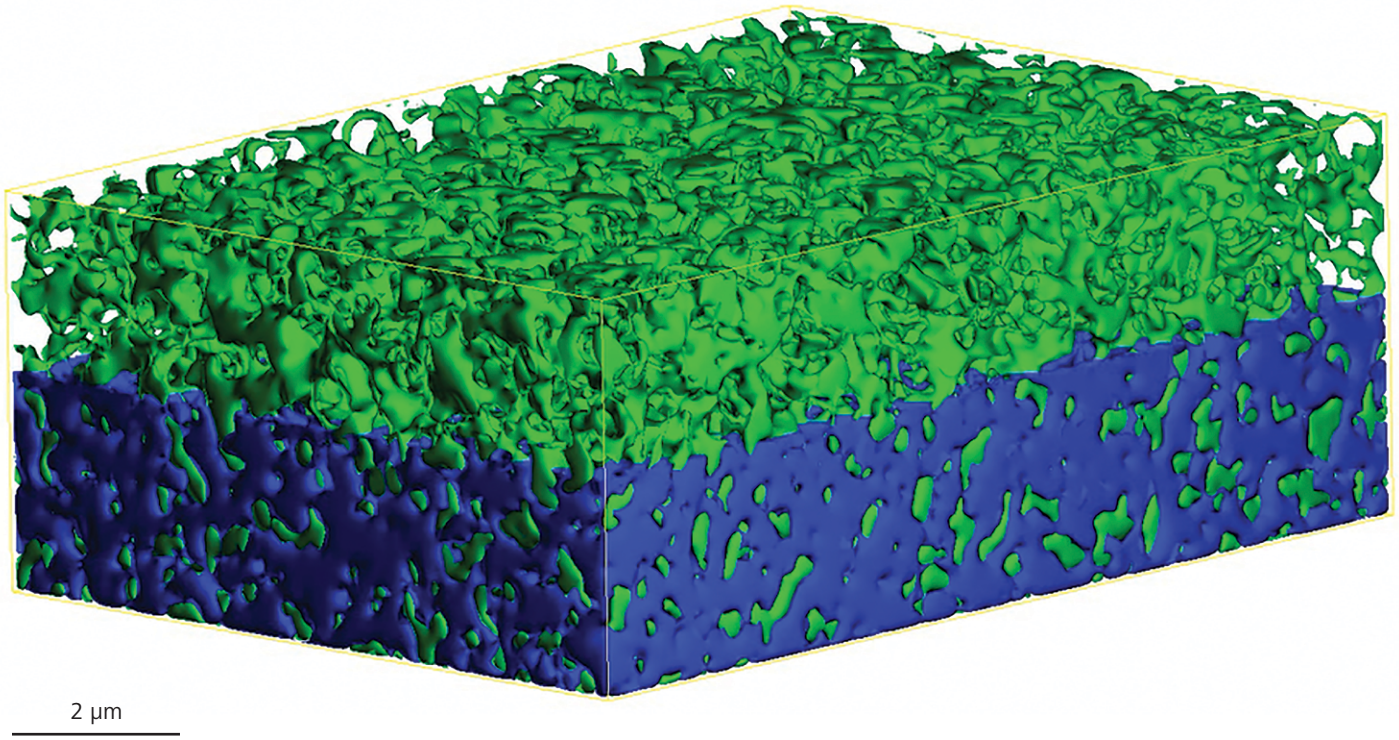

X-ray Nanotomography in the Laboratory

with ZEISS Xradia Ultra 3D X-ray Microscopes

X-ray Nanotomography in the Laboratory

with ZEISS Xradia Ultra 3D X-ray Microscopes

Author: *ZEISS Microscopy*

Date: May 2018

X-ray microscopy (XRM) enables non-destructive 3D investigation of a variety of samples across multiple length scales. Nanoscale XRM with resolution down to tens of nanometers has long been developed at synchrotron radiation facilities, driven by the development of advanced X-ray optics such as Fresnel zone plates. ZEISS Xradia Ultra is the first instrument to bring this capability to the user's own laboratory. In this paper, we discuss the technology behind Xradia Ultra and resulting performance, including X-ray optics, contrast modes and X-ray energy. The paper concludes with application areas and upcoming developments.

Benefits of laboratory based X-ray nanotomography:

- Non-destructive 3D imaging down to 50 nm resolution
- *In situ* and 4D imaging: Observe nanostructural evolution by imaging the same specimen multiple times under varying conditions, or over time
- Multiscale and correlative imaging: Bridge the gap between micro-CT and nanometer resolution, but destructive, electron microscopy techniques
- Contrast for a wide range of materials, from polymers and tissue to rock, ceramics and metals

On the cover: *PEFC Catalyst Layer showing porosity and connected pore space. Sample courtesy Carnegie Mellon University*

Xradia Ultra technology

Optical architecture

The architecture of Xradia Ultra is conceptually equivalent to an optical microscope or a transmission electron microscope (TEM). This architecture is also called transmission X-ray microscope, or TXM.

- A high-brightness X-ray source is focused onto the specimen by a high-efficiency capillary condenser
- A Fresnel zone plate objective forms a magnified image of the specimen on the X-ray camera (detector)
- An optional phase ring can be inserted into the beam path to achieve Zernike phase contrast to visualize features in low absorbing specimens
- As the specimen is rotated, images are collected over a range of projection angles that are then reconstructed into a 3D tomographic dataset

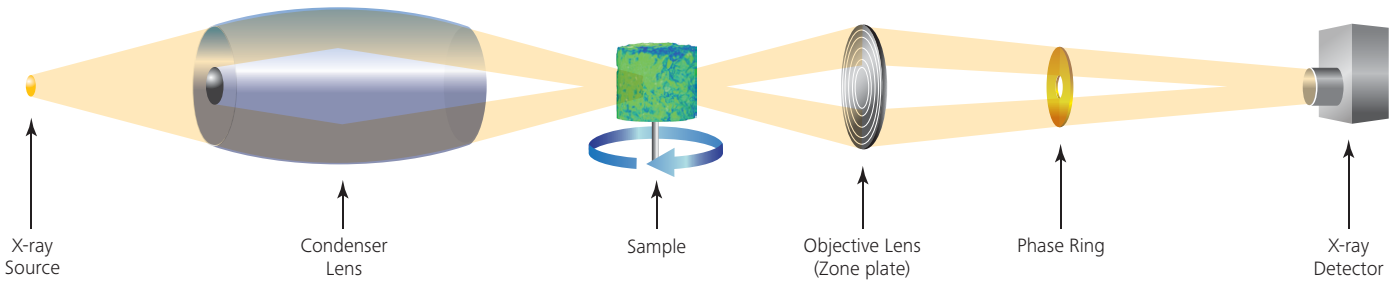

Figure 1: *Optical schematic of Xradia Ultra*

Capillary condensers

The purpose of the condenser lens in a microscope is to provide even illumination of the sample across the entire field of view. Xradia Ultra employs reflective, single bounce capillaries[1] for this purpose that image the X-ray source spot into the sample plane (see Figure 1).

Reflective capillaries have a number of advantages over Fresnel zone plates as condenser lenses in laboratory X-ray microscopes, namely:

- Close to unity focusing efficiency
- Ability to fabricate large numerical aperture (NA) condensers to match NA of high resolution imaging zone plates
- Ability to fabricate large diameter condensers

To prevent excessive blurring of the focal spot, which would result in a loss of X-ray intensity within the field of view, the surface roughness inside the capillary must be controlled to the submicron level.

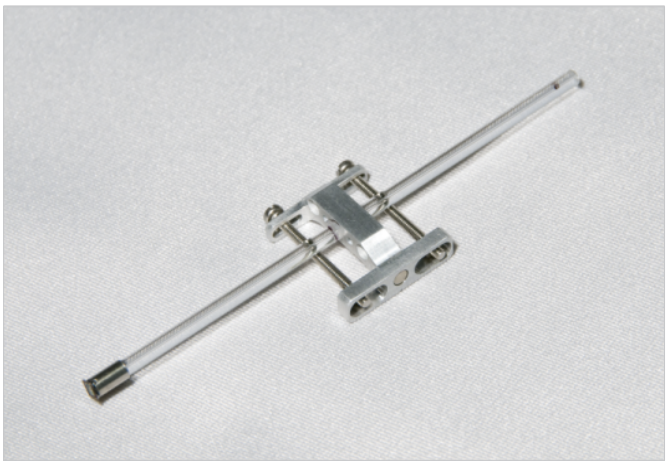

Figure 2: *Capillary condenser*

Fresnel zone plates

Fresnel zone plates are used as microscope objectives to provide a magnified image of the sample on the X-ray camera. Zone plates are circular diffraction gratings with radially decreasing line width, acting as a focusing lens for X-rays[2,3] (see Figure 3). Some optical parameters of zone plates are listed in Appendix B.

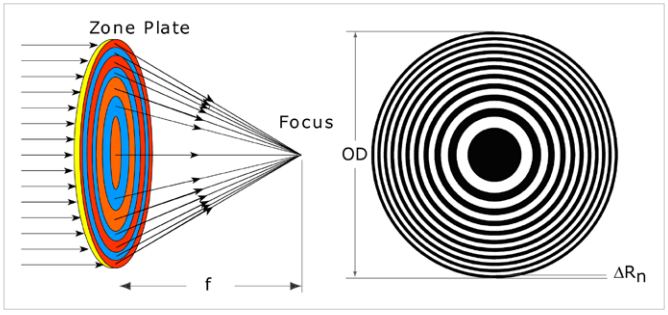

Figure 3: *Top: Schematic of a zone plate.*

Right: *SEM image of a zone plate.*

The spatial resolution that can be achieved, determined by the Numerical Aperture (NA) in the same way as in an optical microscope, is about the same as the width of the finest, outer zones (ΔR_n, typically a few tens of nanometers). At the same time, the zones need to be tall (hundreds of nanometers to more than a micron) to be efficient. This leads to a requirement for very high aspect ratio (ratio of height to width) structures. ZEISS XRM has developed proprietary technology to "stack" and permanently bond zone plates with nanometer accuracy to increase the effective zone height and therefore aspect ratio[4] (see Figure 4).

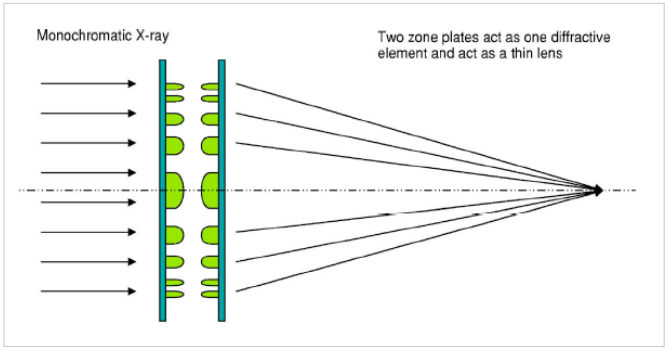

Figure 4: *Schematic of the stacking concept,[4] where two zone plates are bonded together to increase the effective thickness of the zones. Zones need to be narrow (laterally) to achieve high spatial resolution, but thick to achieve high efficiency (which translates into imaging throughput of the X-ray microscope).*

X-ray camera

The X-ray camera in Xradia Ultra is based on a scintillator optically coupled to a CCD detector. This is the same concept employed by the Xradia Versa family of submicron resolution XRMs.

As is illustrated in Figure 5, X-rays are incident on a scintillator, which converts X-rays to visible light. The visible light image is then magnified and projected onto a CCD camera by an optical lens assembly.

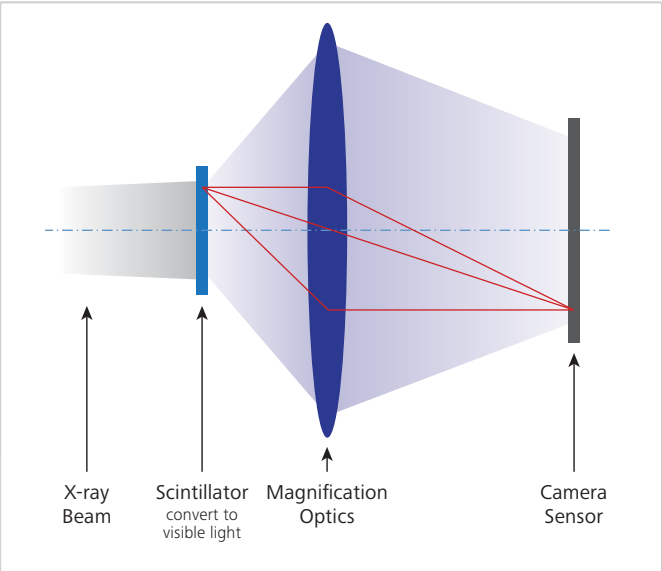

Figure 5: *X-ray camera concept*

Optical performance and spatial resolution

The optical architecture described above achieves *spatial resolution* below 50 nm. The spatial resolution of an imaging system is the smallest distance two features can be separated by to still be distinguishable from one another.[5] Siemens stars, resolution targets with radially decreasing feature size, are commonly used in X-ray microscopy to assess resolution (see Figure 6). Note that spatial resolution is not the same as pixel size (or voxel size, for 3D imaging). While the voxel size needs to be smaller than the desired spatial resolution (it is 16 nm for Xradia Ultra in High Resolution mode at 800X magnification), a small voxel size alone does not help distinguish features if the optical resolution of the instrument is insufficient.[5]

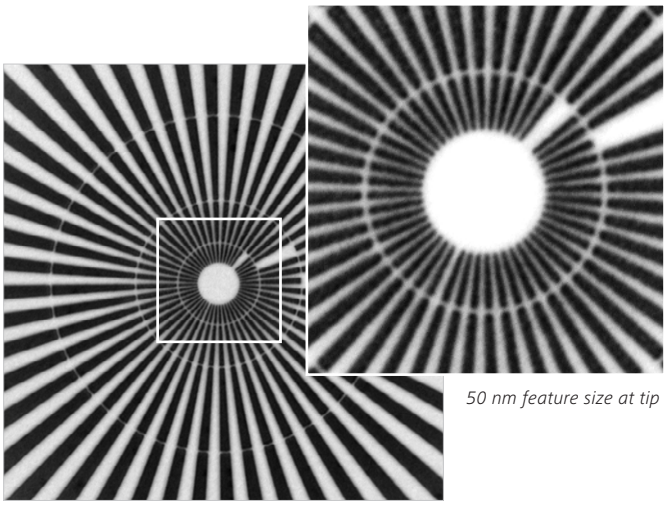

Figure 6: *Spatial resolution of Xradia Ultra, demonstrated using a Siemens star resolution target. The innermost features are 50 nm wide (50 nm lines, 50 nm spaces). Image pixel size is 16 nm.*

X-ray computed tomography (CT)

One of the unique properties of X-rays is their penetration power, i.e. their ability to see through and inside optically opaque, thick specimens. However, a simple two-dimensional X-ray *projection image* through a thick specimen with complex internal structure is often not useful because features overlay each other. Computed tomography (CT), widely used in the medical field, allows the reconstruction of a 3D virtual volume from individual projections. More recently, micro- and nano-CT[6-9] have pushed this technique to much higher resolutions.

In CT, many individual projection images of the specimen are acquired over a range of angles (viewing directions), ideally covering 180 or 360 degrees. Industrial, micro- and nano-CT as well as 3D X-ray microscopes typically rotate the specimen through a stationary X-ray beam for this purpose. This is in contrast to hospital X-ray CT, where the X-ray source and detector are rotated around a stationary patient.

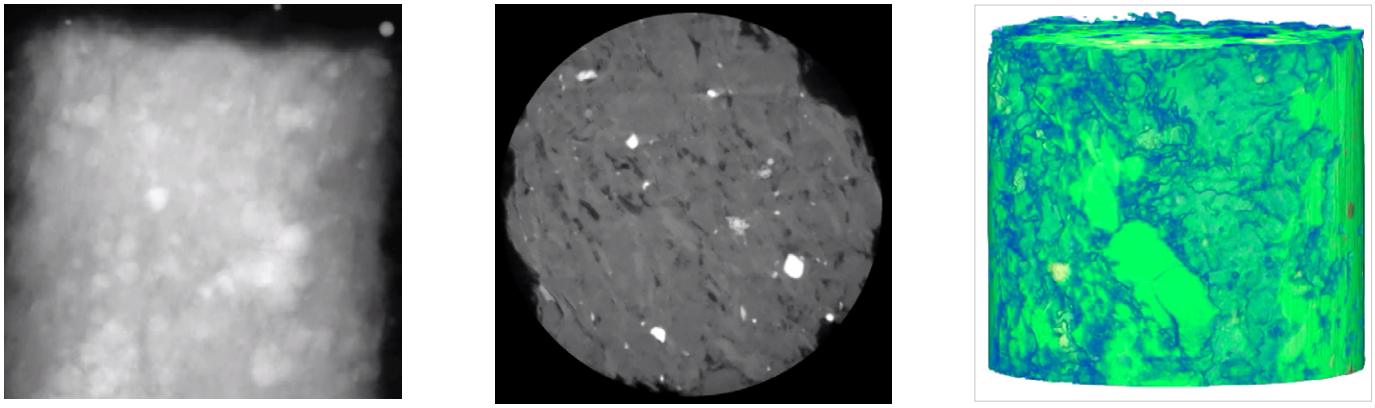

Figure 7: *X-ray computed tomography illustrated using the example of a shale rock sample. Left: Example projection through the specimen. While some interior features are visible, the interior structure cannot be determined in detail from a single projection. Center: A projection series over an angular range of 180 degrees was reconstructed into a virtual volume. The image shows an individual "slice" (virtual cross section) through the specimen. Right: Volume rendering of the reconstructed volume.*

The number of projection images acquired is typically in the hundreds or thousands. Computer algorithms[10] are then used to reconstruct a virtual, 3-dimensional volume of the specimen. The most common algorithms are filtered backprojection (FBP) or Feldkamp-Davis-Krees (FDK, for cone beam CT), although various advanced (e.g., iterative) algorithms exist and can yield better results under certain conditions.

The reconstructed volume can then be viewed "slice by slice" (looking at *virtual cross-sections*), or visualized in 3D using various volume rendering methods (see Figure 7). Commonly, the reconstructed volume is *segmented* into different components based on grayscale or other characteristics. Segmented volumes can be further analyzed quantitatively in terms of porosity, tortuosity, particle size distribution or other properties, or be used as input for advanced modeling algorithms.

The key difference between Xradia Ultra and other micro- or nano-CT instruments is the use of X-ray optics to achieve ultrahigh resolution projections as described above.

Absorption and phase contrast

Microscopes may provide a variety of contrast mechanisms that are sensitive to different properties or components of the specimen and therefore complement each other. In this section, we describe absorption and phase contrast, two contrast modes typically used to visualize morphology of the sample and both available in Xradia Ultra. Other contrast modes available in other types of microscopes (light, electron or synchrotron based X-ray microscopes) include optical or X-ray fluorescence for functional or elemental imaging, diffraction for crystallographic orientation, or spectroscopic contrast mechanism for elemental or chemical imaging.

Absorption contrast

Absorption contrast is essentially shadow contrast, similar to standard medical X-rays. Material that absorbs strongly shows up dark in the image, material that absorbs less shows up bright – like bone vs. tissue in the hospital. Absorption is typically stronger for materials with higher density and/or atomic number. The mechanism is explained in more detail in the section on X-ray source energy below.

Absorption is most often used to image pore networks or other voids (empty space = low/no absorption) in medium to high density materials, such as rock, calcified tissue, ceramics or metals. In a multi-phase or composite material, if the components are of sufficiently different density, absorption contrast can also be used to separate the materials (e.g. ceramic-metallic composites, or cermets).

Phase contrast

Phase contrast[11] is primarily used for imaging materials that have low absorption, or to differentiate materials of similar density. Phase contrast uses the optical effect of refraction rather than absorption. It is very sensitive to the transition between different materials (edge enhancement). Note that the term "phase" here refers to the phase shift of an optical wave, and not to material phases (like crystallographic phases).

Phase contrast is essential when imaging materials of low density or atomic number, such as polymers or soft tissue, since absorption contrast is typically very weak. Figure 8 shows an example of a polymer membrane imaged in phase contrast.

Due to the edge enhancement properties of phase contrast, it is also well suited to detect small features close to the resolution limit, such as fine cracks and defects, in more strongly absorbing material. It may be used as an initial survey mode to find small features prior to 3D imaging in absorption contrast. On the other hand, these same edge enhancement properties mean that different gray scales in the image may not correspond directly to different materials. In such a case, phase contrast may be more suitable to detect and visualize small features, whereas absorption contrast is more suitable to quantify and segment features based on gray scale thresholding. A comparison of absorption and phase contrast for a sample of shale rock is shown in Figure 9.

Multiple implementations of phase contrast imaging have been developed over time for different microscope architectures. Xradia Ultra uses the Zernike principle to achieve phase contrast (see Figure 10). This principle was invented by Frits Zernike in the 1930s for light microscopes,[12] for which he received the Nobel Prize in 1953.[13]

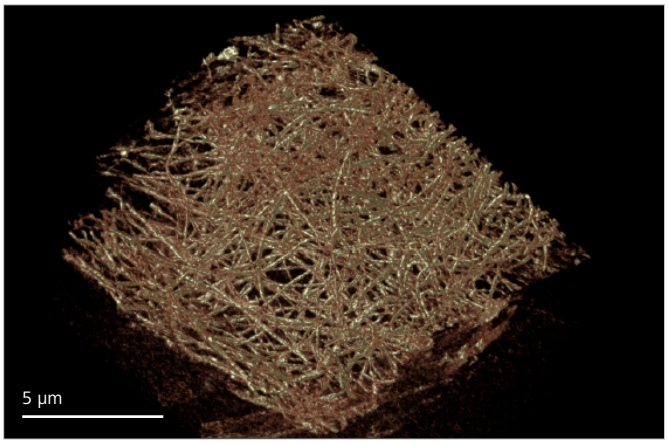

Figure 8: *Polymer fibers in a desalination membrane, imaged in phase contrast. Such low-Z materials are essentially transparent to multi-keV X-rays and therefore not able to be visualized in absorption contrast.* Sample courtesy of Industrial Technology Research Institute (ITRI).

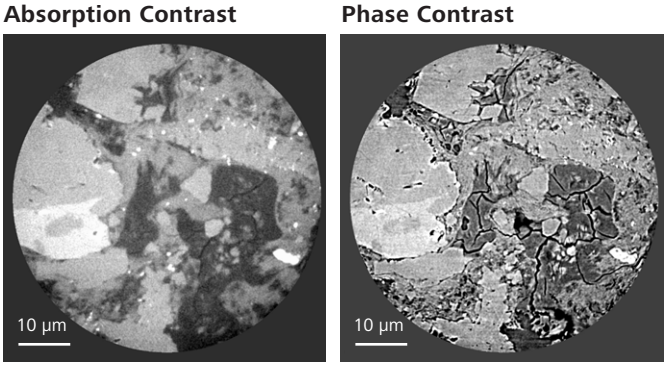

Figure 9: *Comparison of absorption and phase contrast for a shale rock sample. In absorption contrast (left), the grayscales in the image directly represent different materials or material phases in the sample, which makes it more suitable for image segmentation. Phase contrast (right) visualizes fine cracks much more clearly.*

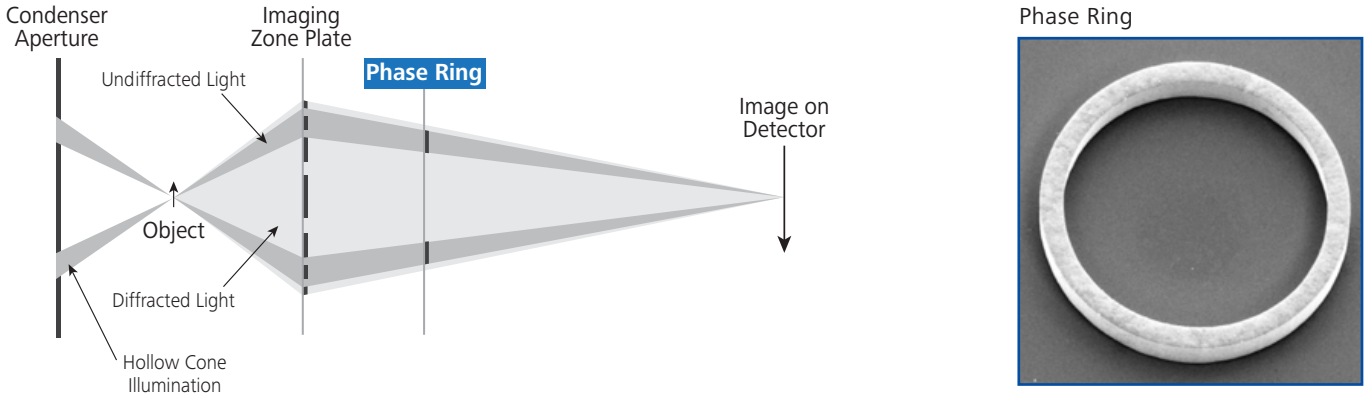

Figure 10: *Left: Illustration of Zernike phase contrast. The sample is illuminated by a hollow cone of X-rays. A phase ring is inserted in the back focal plane of the objective zone plate. The "undiffracted light" (X-rays that have not interacted with the sample) passes through the phase ring and is phase shifted by a quarter wavelength. "Diffracted light" (X-rays that have interacted with the sample and therefore have been scattered off the direct path) does not pass through the phase ring. In the detector plane, the diffracted and undiffracted light combine (interfere), which turns phase shifts into intensity variations. Right: SEM image of a phase ring.*

X-ray source energy

3D data acquisition times in a laboratory based nanoscale XRM are on the time scale of hours. Therefore, optimizing throughput is essential to make the most productive use of the system. In this section, we will review how the two different X-ray source options, 5.4 keV for Xradia 810 Ultra and 8 keV for Xradia 800 Ultra, differ in terms of imaging properties and performance for different materials to be imaged. To do so, we will review how X-rays get absorbed in matter[14] and what that means for the resulting image contrast and feature detectability. We will explain that in the context of absorption contrast, although the concepts apply similarly to phase contrast. For further details, see Ref. 15, which illustrates contrast, noise and detectability in the context of medical CT.

X-ray absorption in matter

Absorption of X-rays in matter follows the Lambert-Beer law:

$$I = I_0 \exp(-t/t_0)$$

where I is the intensity after propagation distance t, I_0 is the incident intensity, and t_0 is the *absorption length* of the material in question at a given X-ray energy. t_0 is the distance after which the intensity falls to $1/e = 37\%$ of the incident value. Sometimes, the *absorption coefficient* $\mu = 1/t_0$ is used instead.

The absorption length is a function of the material, its density and the X-ray energy. Generally, the absorption length increases with energy (i.e., harder X-rays are more penetrating), and decreases with density and atomic number Z (i.e., heaver materials are more strongly absorbing).

Looking at the two specific X-ray source energies available for Xradia Ultra, the absorption length is generally longer at 8 keV than at 5.4 keV. There are a few exceptions (specifically vanadium, chromium, manganese, iron and cobalt), which have so-called absorption edges (discontinuities in the absorption length due to the specific atomic energy levels) in between the two energies. A few examples are listed in Table 1 below. To provide for sufficient penetration for imaging, the sample thickness should be at most ~2x the absorption length.

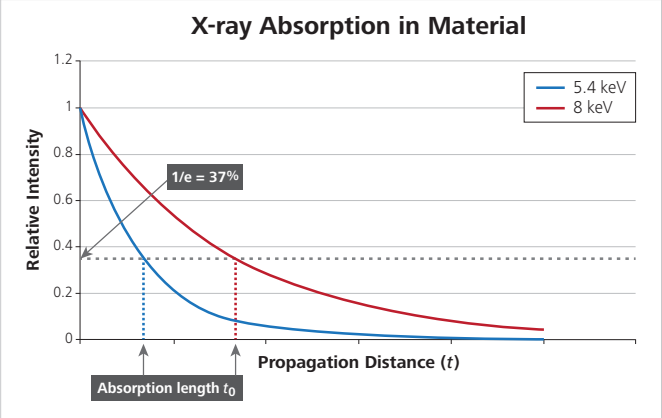

Figure 11: *Schematic illustration of X-ray absorption in matter following the Lambert-Beer law. After a propagation distance t_0 (which is a function of X-ray energy), the intensity drops to 37% of its incident value.*

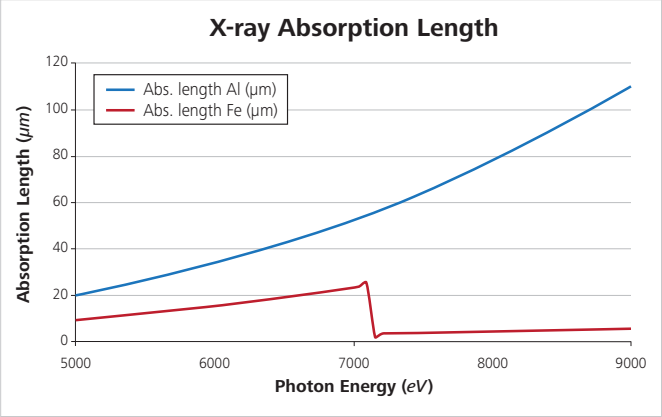

Figure 12: *Illustration of X-ray absorption length for two example elements. Generally, absorption length is longer for lighter elements (aluminum, Al) compared to heavier elements (iron, Fe). Furthermore, absorption length typically increases with energy, except for so-called absorption edges, which are discontinuities in the absorption spectrum. This is illustrated for the example of iron, which has an absorption edge around 7.1 keV photon energy.*

Sample	5.4 keV	8.0 keV
Iron*	11.7 µm	4.16 µm
Aluminum	24.8 µm	77.6 µm
PMMA	397 µm	1337 µm
$CaCO_3$	16.5 µm	48.7 µm
Silicon	22.4 µm	69.6 µm
Tungsten	1.14 µm	3.11 µm

*Note: Iron is an exception to the rule that 8 keV X-rays can penetrate further than 5.4 keV X-rays. This is because of the iron X-ray absorption edge at 7.1 keV, above which penetration drops drastically.

Table 1: *Approximate X-ray absorption length for select materials. Exact values will depend on composition and density. Note that X-ray penetration will be larger if material is porous.*

Contrast

Contrast is the difference in light intensity that makes different features in an image distinguishable from one another. To be able to detect a feature, it must both be resolved (see *Optical Performance and spatial resolution* above) and have sufficiently strong contrast compared to its surroundings.

As described above, lower energy X-rays are generally absorbed more strongly and therefore will provide higher contrast. Thus, as long as transmission remains sufficient, resulting image quality and/or throughput will be greatly improved at 5.4 keV X-ray energy compared to 8 keV. However, for materials of higher density (such as most metals, but note the exception of iron explained above), or thick specimens, the higher X-ray energy of 8 keV may be needed for sufficient transmission (see Figure 13). The contrast difference is illustrated on a real world sample in Figure 14. 5.4 keV X-rays are absorbed more strongly than 8 keV, resulting in higher contrast and therefore better detectability.

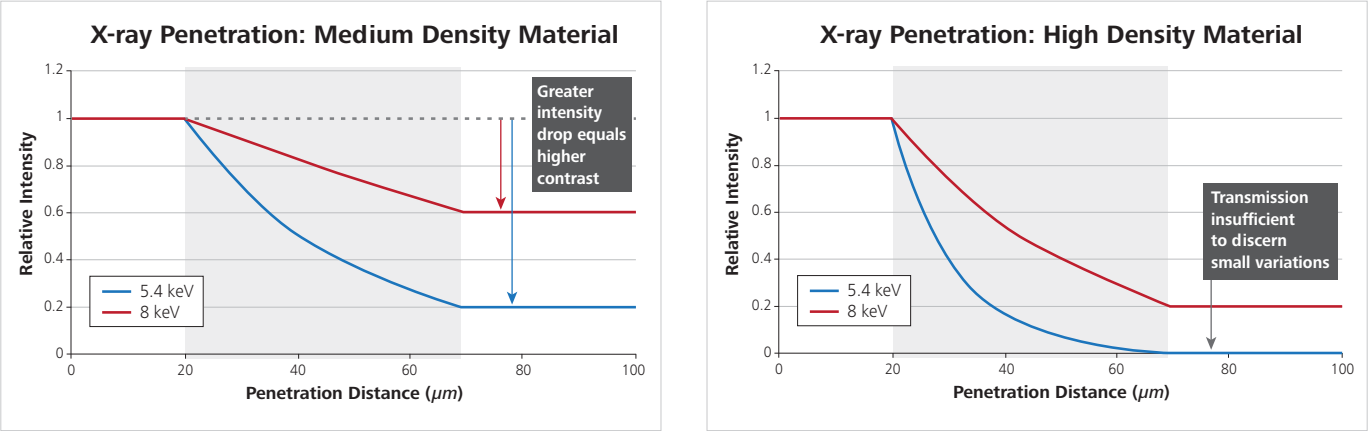

Figure 13: *Illustration of 5.4 vs. 8 keV X-ray energy. Left: The greater intensity drop of 5.4 keV X-rays leads to higher contrast (and therefore higher imaging throughput). Right: If absorption becomes too strong (dense material or sample too thick), transmission at 5.4 keV may be too low to discern small variations, in which case 8 keV is preferred.*

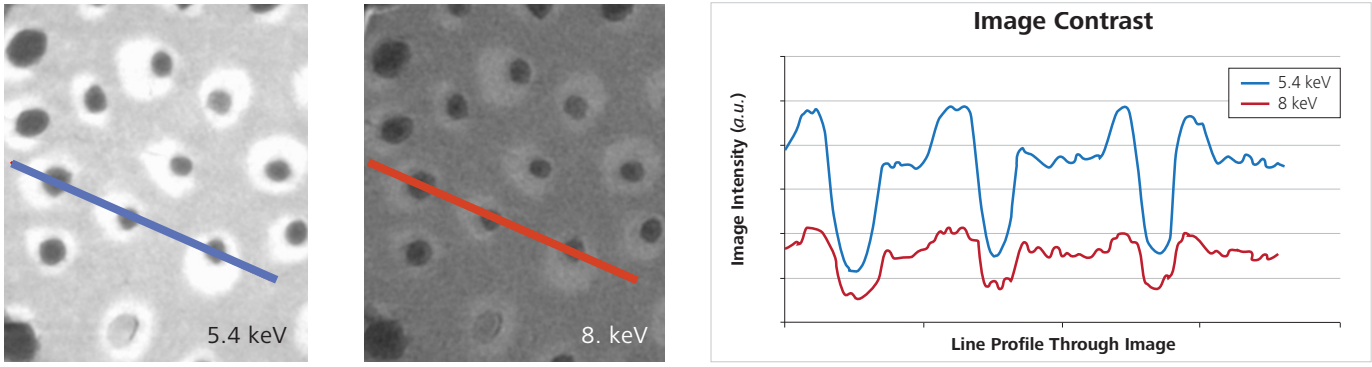

Figure 14: *Contrast difference between 5.4 and 8 keV illustrated using virtual cross-sections of a dentin sample. The lower X-ray energy of 5.4 keV provides stronger contrast between the bulk intertubular dentin (medium gray), peritubular dentin (light) and tubules (dark). Note that the images follow the convention of displaying higher density materials in light colors and lower density (air) in dark. The plot on the right shows an intensity profile across the lines indicated in the images. It is evident that the contrast (intensity difference) is stronger at 5.4 keV than at 8 keV.*

Noise

Imaging, like any measurement process, introduces noise. Noise is a random fluctuation of the measured value around the expected, or "true" value. That means, even if we were to image a perfectly uniform material, the measured intensity values of different pixels (or, the same pixel in multiple measurements) would not be exactly the same.

While multiple noise sources exist in an X-ray microscope, we will concentrate here on shot noise, which is intrinsic to the measurement of discrete particles such as X-ray photons. Shot noise follows a Poisson distribution, which means if we expect to measure an average number of n photons in many measurements of the same type, the distribution of actual measurements will have a standard deviation (noise) of $\sqrt{n}$ (see Figure 15).

We can then define the Signal-to-Noise Ratio (SNR) as the ratio of expected number of photons and noise:

$$\mathrm{SNR} = {}^{\mathrm{Signal}}/_{\mathrm{Noise}} = {}^{n}/_{\sqrt{n}} = \sqrt{n}$$

In other words, by increasing the exposure time and therefore counting more X-ray photons, we can decrease the noise level *relative to the measured signal*. This is in analogy to photography, where in the case of low light, longer exposure times are used to decrease noise. However, the improvement follows a square root relationship, i.e. we have to measure four times as long to double the SNR.

This concept is illustrated again for the case of dentin in Figure 16. Here, both images were acquired using 5.4 keV X-ray source energy, meaning the contrast between the different features is the same. However, it can be seen that the noise is much lower for the longer exposure.

Putting it all together:

Contrast to Noise Ratio and imaging throughput

So what does all this mean for general image quality and detectability of features in an image? Ultimately, what counts is the Contrast-to-Noise Ratio (CNR) of the features of interest relative to the surroundings. CNR can be increased by either increasing contrast or decreasing noise. In other words, even in the case of lower contrast we can detect features by exposing longer and therefore decreasing noise.

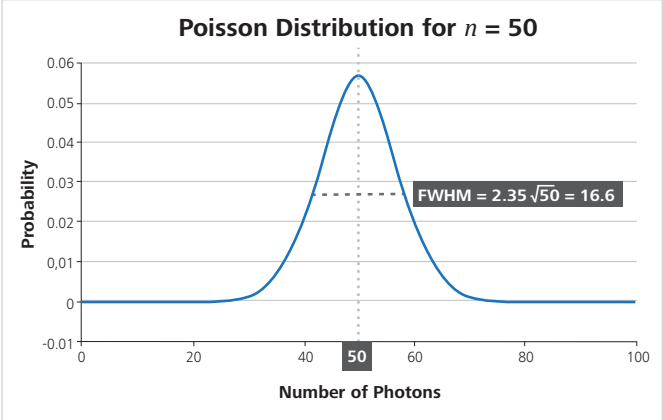

Figure 15: *Illustration of Poisson distribution. Assuming we expect to measure a mean of n=50 photons in many measurements of the same type, the actual number measured in a single measurement will vary from about 30 to 70 based on the distribution shown. It can be shown that the full width at half maximum (FWHM) of this distribution is* $\mathrm{FWHM} = 2.35\sqrt{n}$, *or* $\mathrm{FWHM} = 16.6$ *in this case.*

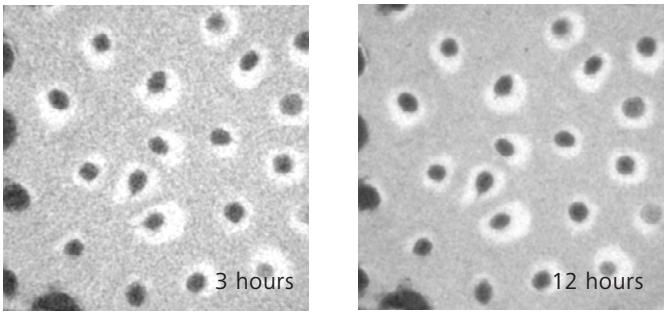

Figure 16*: Virtual cross section of dentin sample from a 3 hr tomogram (left) and a 12 hour tomogram (right) at 5.4 keV X-ray energy. It is evident that the longer exposure leads to lower noise.*

However, if we can increase contrast by using a more suitable X-ray energy, we can achieve sufficient CNR with shorter exposure times, which is generally preferred.

Looking back at Figure 16 again, note that contrast is the same in both images because they were both acquired at 5.4 keV X-ray energy. However, CNR is clearly improved with the 12 hour exposure.

Conclusions

We have seen that for most materials, 5.4 keV X-rays are absorbed more strongly than 8 keV X-rays, leading to higher contrast and therefore higher imaging throughput. In other words, equivalent image quality can be achieved with shorter exposure times. If fact, it has been shown that for samples such as rock or calcified tissue, the same contrast to noise ratio (image quality) can be achieved about 10 times faster using a 5.4 keV X-ray source compared to 8 keV.

On the other hand, for samples made of higher-Z ("heavier") material, 8 keV might be needed to provide sufficient penetration. Ultimately, the preferred source energy varies by application.

Furthermore, for a given experiment, it is important to consider what image quality is sufficient. It may be more productive to measure multiple samples at lower CNR in a given time frame than just a single one at higher CNR, as long as the results allow detecting and quantifying the features of interest as required.

Mechanical architecture

To achieve 50 nm resolution in a 3D measurement taking several hours, the microscope needs to be mechanically stable over that time frame. The following design features are implemented in Xradia Ultra to achieve that:

- Xradia Ultra is built on a low vibration platform to isolate the optical system from external vibrations
- Careful thermal engineering and calibration prevents or corrects thermal drifts on the scale of tens of nanometers between specimen and optics
- Motion errors of the rotation stage are measured and corrected for by a novel run-out correction system[16]
- The precision motion control system comprises 26 axes of motion to position and align the X-ray optics, sample, optical alignment microscope and other components

Application areas

In the following, we list a number of applications where Xradia Ultra and its predecessor models (Xradia nanoXCT and UltraXRM) have been used to provide 3D nanostructure data.

Materials research

- Li-ion battery electrodes[17-19]
- Polymer electrolyte fuel cell (PEFC) electrodes[20-22]
- Solid oxide fuel cell (SOFC) electrodes[23]
- 3D-ordered macroporous materials for CO_2 capture[24]
- Osmosis membranes[25]
- Alloys[26]
- Superconducting materials[27]
- Nanocomposites[28]
- Cement[29]
- Subsurface coatings[30]
- High voltage insulators[31]

Life and environmental science

- Unstained tissue[32]
- Nanoparticle uptake in protozoa or soybean roots[33,34]
- Pharmaceutical particles[35]
- Bone and dentin

Natural resources

- Digital rock physics (DRP)[36,37] or general rock characterization,[38,39] e.g. for carbonate rock, shale rock, or tight sand

Electronics

- Voids and extrusions in through-silicon via (TSV)[40,41]

Summary and outlook

Nanoscale 3D X-ray microscopy is the only technique that can achieve spatial resolution down to 50 nm, non-destructively, on samples of tens to hundreds of microns in size. As such, it is particularly well suited to 4D and *in situ* experiments, where the same sample is imaged multiple times over time or under varying conditions, allowing studying microstructural evolution. Furthermore, nanoscale 3D XRM covers a unique length scale in a correlative suite of techniques, between micron/submicron XRM or micro-CT, where larger samples can be studied with resolution down to one micron or slightly below, and serial sectioning using electron microscopy, where smaller volumes can be studied with nanometer resolution, but destructively.

In this White Paper, we described the technology behind Xradia Ultra, the only laboratory based nanoscale X-ray microscope. Resolution down to 50 nm is achieved using X-ray focusing optics such as reflective capillary condensers and Fresnel zone plate objective lenses. Absorption and phase contrast modes allow imaging of a wide variety of materials. Demonstrated applications cover a wide range of examples from materials research, life and environmental sciences, natural resources and electronics. Emerging techniques include *in situ* imaging, for example under mechanical load, 4D imaging, such as monitoring corrosion, and correlative imaging across multiple length scales and using different but complementary techniques.

Appendix A: Why use X-ray optics?

The vast majority of laboratory-based X-ray microscopes and micro CT systems use the principle of cone beam projection through the sample, followed by X-ray detection on a 2D detector. Rapid developments in the last decade have pushed the achievable spatial resolution down to about one micron and below. Two concepts are commonly used[5] (see Figure 17).

- Conventional micro CT systems typically use a small spot X-ray source and a flat panel detector with relatively large pixels (~100 µm). To achieve voxel sizes below one micron, a large geometric magnification (>100x) and therefore very small source-to-sample distance is required.
- ZEISS Xradia Versa architecture uses a two-stage (geometric + optical) magnification. The optical magnification stage effectively provides a small pixel (down to <500 nm) detector. Voxel sizes below one micron can be achieved with low geometric magnification (<10x) and working distances of several centimeters.

While both of these concepts keep pushing spatial resolution further below one micron (currently ~600-700 nm), it is ultimately limited by factors such as achievable X-ray spot size at sufficient power, X-ray detector resolution and practical limitations of acceptable exposure times to achieve sufficient signal-to-noise ratio. It can be shown[42] that at resolution levels below about 500 nm, a projection based architecture becomes impractical. To achieve spatial resolution higher than that and into the sub-100 nm regime, a lens-based architecture using X-ray focusing optics is required.

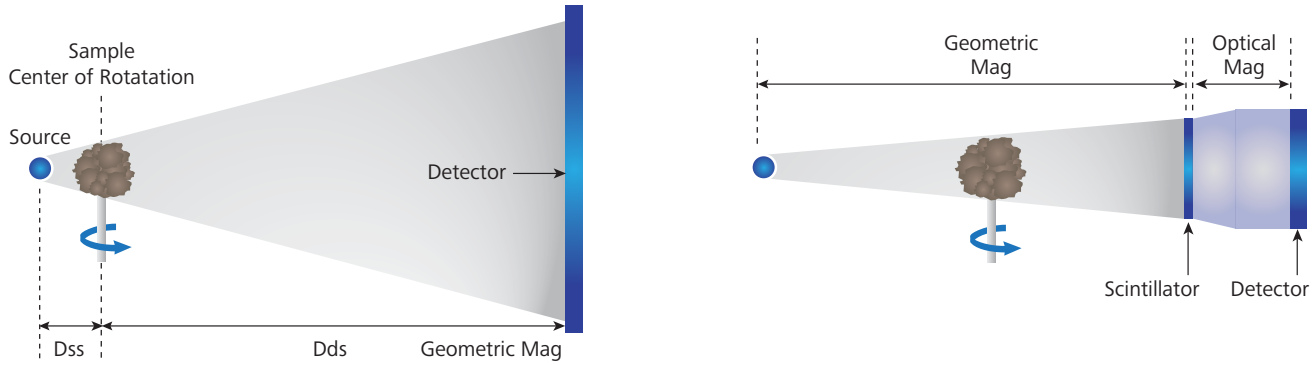

Figure 17: *(Left) Conventional micro CT architecture using a large pixel detector and high geometric magnification to achieve high resolution. This requires a small spot X-ray source to avoid penumbral blurring, and small source to sample distance (working distance) to achieve small voxel sizes. Resolution degrades quickly as the sample is moved away from the source. (Right) ZEISS XRM architecture using two-stage magnification. Moderate geometric magnification is followed by switchable optical magnification. This relaxes the need for high geometric magnification and allows for longer working distance, which is advantageous in the case of interior tomography (imaging a small interior subregion of a large sample at high resolution), and when using in situ sample environments.*

Appendix B: Fresnel zone plates

The properties of a zone plate can be specified by three parameters such as the diameter D, the outer zone width ΔR_n and the wavelength λ.

Then, some other quantities of interest are the number of zones N

$N = {}^{D}/_{4\Delta R_n}$

the focal length f

$f = {}^{D\,\Delta R_n}/_{\lambda}$

and the numerical aperture

$NA = {}^{\lambda}/_{2\,\Delta R_n}$

Note that the relationship between photon energy E and wavelength λ is given by

$E = {}^{hc}/_{\lambda} = {}^{1239.842\ eV\cdot nm}/_{\lambda}$

where $hc = 1239.842\ eV\cdot nm$ is the product of Planck's constant h and the speed of light c.

The spatial resolution achievable by a Fresnel zone plate is determined by the outer zone width ΔR_n.

Specifically, for uniform plane-wave illumination the transverse resolution δ_t according to the Rayleigh criterion is given by Abbe's law:

$\delta_t = {}^{0.61\lambda}/_{NA} = 1.22\,\Delta R_n$

The depth of focus, or longitudinal resolution δ_l, is

$\delta_l = \pm\,{}^{2\Delta R_n{}^2}/_{\lambda}$

References:

[1] X Zeng, et al., "Ellipsoidal and parabolic glass capillaries as condensers for x-ray microscopes." *Appl. Opt.* 47 (2008), 2376-2381. DOI: 10.1364/AO.47.002376

[2] J Kirz, "Phase zone plates for x rays and the extreme uv." *J. Opt. Soc. Am.* 64 (1974), 301-309. DOI: 10.1364/JOSA.64.000301

[3] AG Michette, *Optical Systems for Soft X Rays* (New York: Plenum, 1986)

[4] Y Feng, et al., "Nanofabrication of high aspect ratio 24 nm x-ray zone plates for x-ray imaging applications." *J. Vac. Sci. Technol. B* 26 (2007). DOI: 10.1116/1.2789447

[5] "Resolution of a 3D X-ray Microscope," Carl Zeiss X-ray Microscopy Technical Note, available for download at: http://info.xradia.com/rs/270-LXH-014/images/TechNote_Resolution.pdf

[6] SR Stock, *MicroComputed Tomography: Methodology and Applications* (CRC Press, 2008)

[7] SR Stock, "X-ray microtomography of materials." *Int. Mater.* Rev. 44 (1999), 141-164-181. DOI: 10.1179/095066099101528261

[8] SR Stock, "Recent advances in X-ray microtomography applied to materials." *Int. Mater.* Rev. 53 (2008), 129. DOI: 10.1179/174328008X277803

[9] PJ Withers, "X-ray nanotomography." *Mater Today* 10 (2007), 26-34. DOI: 10.1016/S1369-7021(07)70305-X

[10] AC Kak and M Slaney, *Principles of Computerized Tomographic Imaging* (Society of Industrial and Applied Mathematics, 2001)

[11] A Momose, "Recent Advances in X-ray Phase Imaging." *Jpn. J. Appl. Phys.* 44 (2005), 6355-6367. DOI: 10.1143/JJAP.44.6355

[12] F Zernike, "Das Phasenkontrastverfahren bei der mikroskopischen Beobachtung." *Z. Techn. Physik* 16/11 (1935), 454-457

[13] http://www.nobelprize.org/nobel_prizes/physics/laureates/1953/

[14] D Attwood, *Soft X-rays and Extreme Ultraviolet Radiation* (Cambridge University Press, 1999)

[15] www.impactscan.org/slides/impactcourse/noise_and_low_contrast_resolution/

[16] J Wang, et al., "Automated markerless full field hard x-ray microscopic tomography at sub-50nm 3-dimension spatial resolution." *Appl. Phys. Lett.* 100 (2012), 143107. DOI: 10.1063/1.3701579

[17] DS Eastwood, et al., "The application of phase contrast X-ray techniques for imaging Li-ion battery electrodes." *Nucl. Instrum. Methods Phys. Res., Sect. B* 324 (2014), 118-123. DOI: 10.1016/j.nimb.2013.08.066

[18] PR Shearing et al., "Multi Length Scale Microstructural Investigations of a Commercially Available Li-Ion Battery Electrode." *J. Electrochem. Soc.* 159 (2012), A1023-A1027. DOI: 10.1149/2.053207jes

[19] B Yan, et al., "Three Dimensional Simulation of Galvanostatic Discharge of $LiCoO_2$ Cathode Based on X-ray Nano-CT Images." *J. Electrochem. Soc.* 159 (2012), A1604-A1614. DOI: 10.1149/2.024210jes

[20] S Litster, et al., "Morphological Analyses of Polymer Electrolyte Fuel Cell Electrodes with Nano-Scale Computed Tomography Imaging." *Fuel Cells* 13 (2013), 935-945. DOI: 10.1002/fuce.201300008

[21] WK Epting et al., "Resolving the Three-Dimensional Microstructure of Polymer Electrolyte Fuel Cell Electrodes using Nanometer-Scale X-ray Computed Tomography." *Adv. Funct. Mat.* 22 (2012), 555-560. DOI: 10.1002/adfm.201101525

[22] WK Epting and S. Litster, "Effects of an agglomerate size distribution on the PEFC agglomerate model." *Int. J. Hydrogen Energy* 37 (2012), 8505-8511. DOI: 10.1016/j.ijhydene.2012.02.099

[23] JR Izzo, et al., "Nondestructive Reconstruction and Analysis of SOFC Anodes Using X-ray Computed Tomography at Sub-50 nm Resolution." *J. Electrochem. Soc* 155 (2008), B504-B508. DOI: 10.1149/1.2895067

[24] H He, et al., "Three-Dimensionally Ordered Macroporous Polymeric Materials by Colloidal Crystal Templating for Reversible CO_2 Capture.", *Adv. Funct. Mat.* 23 (2013), 4720-4728. DOI: 10.1002/adfm.201300401

[25] SS Manickam, et al., "Pore structure characterization of asymmetric membranes: Non-destructive characterization of porosity and tortuosity." *J. Membr. Sci.* 454 (2014), 549-554. DOI: 10.1016/j.memsci.2013.11.044

[26] BM Patterson, et al., "Laboratory micro- and nanoscale X-ray tomographic investigation of Al–7 at.%Cu solidification structures." *Mater. Charact.* 95 (2014), 18-26. DOI: 10.1016/j.matchar.2014.06.004

[27] JH Kim et al., "Microscopic role of carbon on MgB_2 wire for critical current density comparable to NbTi." *NPG Asia Mater.* 4 (2012), e3. DOI: 10.1038/am.2012.3

[28] V Stepanov et al., "Structural Characterization of RDX-Based Explosive Nanocomposites." *Propell. Explos. Pyrot.* 38 (2013), 386-393. DOI: 10.1002/prep.201200151

[29] N Bossa et al., "Micro- and nano-X-ray computed-tomography: A step forward in the characterization of the pore network of a leached cement paste." *Cement Concrete Res.* 67 (2015), 138-147. DOI: 10.1016/j.cemconres.2014.08.007

[30] NL Cordes et al., "Non-destructive elemental quantification of polymer-embedded thin films using laboratory based X-ray techniques." *Spectrochim. Acta B* 101 (2014), 320-329. DOI: 10.1016/j.sab.2014.09.016

[31] R Schurch et al., "Imaging and Analysis Techniques for Electrical Trees using X-ray Computed Tomography." *IEEE T. Dielect. El. In.* 21 (2014), 53-63. DOI: 10.1109/TDEI.2014.6740725

[32] LA Walton, et al., "Morphological Characterisation of Unstained and Intact Tissue Micro-architecture by X-ray Computed Micro- and Nano-Tomography." *Sci. Rep.* 5 (2015), 10074. DOI: 10.1038/srep10074

[33] RE Mielke, et al., "Differential Growth of and Nanoscale TiO_2 Accumulation in Tetrahymena thermophila by Direct Feeding versus Trophic Transfer from Pseudomonas aeruginosa." *Appl. Environ. Microbiol.* 79 (2013), 5616-5624. DOI: 10.1128/AEM.01680-13

[34] JH Priester, et al., "Soybean susceptibility to manufactured nanomaterials with evidence for food quality and soil fertility interruption." *Proc. Natl. Acad. Sci. U.S.A.* 109 (2012), E2451-E2456. DOI: 10.1073/pnas.1205431109

[35] J Wong, et al., "NanoXCT: A Novel Technique to Probe the Internal Architecture of Pharmaceutical Particles." *Pharm. Res.* 31 (2014), 3085-3094. DOI: 10.1007/s11095-014-1401-8

[36] J Dvorkin et al., "From micro to reservoir scale: Permeability from digital experiments." *The Leading Edge* 28 (2009), 1446-1452. DOI: 10.1190/1.3272699

[37] J Tölke, et al., "Computer simulations of fluid flow in sediment: From images to permeability." *The Leading Edge* 29 (2010), 68-74. DOI: 10.1190/1.3284055

[38] B Bai et al., "Multi-scale method of Nano(Micro)-CT study on microscopic pore structure of tight sandstone of Yanchang Formation, Ordos Basin." *Petrol. Expl. Dev.* 40 (2013), 354-358. DOI: 10.1016/S1876-3804(13)60042-7

[39] S. Wu et al., "Characteristics of lacustrine shale porosity evolution, Triassic Chang 7 Member, Ordos Basin, NW China." *Petrol. Expl. Dev.* 42 (2015), 185-195. DOI: 10.1016/S1876-3804(15)30005-7

[40] LW Kong et al., "3D-interconnect: Visualization of extrusion and voids induced in copper-filled through-silicon vias (TSVs) at various temperatures using X-ray microscopy." *Microelectron. Eng.* 92 (2012), 24-28. DOI: 10.1016/j.mee.2011.04.012

[41] LW Kong et al., "Applying x-ray microscopy and finite element modeling to identify the mechanism of stress-assisted void growth in through-silicon vias." *J. Appl. Phys.* 110 (2011), 053502. DOI: 10.1063/1.3629988

[42] M Feser. "Resolution Limits of Projection X-ray Microscopy and Tomography." *In preparation, to be published in Proc. of SPIE* 9592 (2015).

Carl Zeiss Microscopy GmbH
07745 Jena, Germany
microscopy@zeiss.com
www.zeiss.com/microscopy